Neurobiology of Disease

Altered Cortical Trigeminal Fields Excitability by Spreading Depolarization Revealed with *in Vivo* Functional Ultrasound Imaging Combined with Electrophysiology

Laurence Bourgeais-Rambur,[1,2,3] Laurianne Beynac,[1,2] Jean-Charles Mariani,[1,4] Mickael Tanter,[5] Thomas Deffieux,[5] Zsolt Lenkei,[1,4] and Luis Villanueva[1,6]

[1]Université de Paris, Institut National de la Santé et de la Recherche Médicale U1266, Institute of Psychiatry and Neuroscience of Paris, 75014 Paris, France , [2]Electrophysiology-Functional Ultrasound imaging Technical Core, Institute of Psychiatry and Neuroscience of Paris, 75014 Paris, France, [3]Team Pathogenesis of Small Vessel Diseases of the Brain, [4]Team Dynamics of Neuronal Structure in Health and Disease, [5]Institut National de la Santé et de la Recherche Médicale U1273, Physics for Medicine Technological and Research Accelerator in Biomedical Ultrasound, Centre National de la Recherche Scientifique UMR 8361, École Supérieure de Physique et de Chimie Industrielles de la Ville de Paris, Université Paris Science et Lettres, 70512 Paris, France, and [6]Team Imaging Biomarkers of Brain Disorders (IMA-Brain)

Spreading depolarization, usually termed cortical spreading depression has been proposed as the pathophysiological substrate of migraine aura and as an endogenous trigger of headache pain. The links between neurovascular coupling and cortical craniofacial nociceptive activities modulated by SD were assessed by combining *in vivo* local field potential (LFP) recordings in the primary somatosensory cortex (S1) with functional ultrasound imaging of S1 and caudal insular (INS) cortices of anesthetized male rats. A single SD wave triggered in the primary visual cortex elicited an ipsilateral, quadriphasic hemodynamic and electrophysiological response in S1 with an early phase consisting of concomitant increases of relative cerebral blood volume (rCBV) and LFPs. A transient hypoperfusion was then correlated with the beginning of the neuronal silence, followed by a strong increase of rCBV, whereas synaptic activities remained inhibited.

LFPs and rCBV recovery period was followed by a progressive increase in S1 and INS baseline activities and facilitation of cortical responses evoked by periorbital cutaneous receptive field stimulation. Sensitization of cortical ophthalmic fields by SD was bilateral, occurred with precise spatiotemporal profiles, and was significantly reduced by pretreatment with an NMDA antagonist. Combined high-resolution assessing of neurovascular coupling and electrophysiological activities has revealed a useful preclinical tool for deciphering central sensitization mechanisms involved in migraine attacks.

Key words: **cortical sensitization; headache; migraine; pain; spreading depolarization; trigeminal**

Significance Statement

A crucial unsolved issue is whether visual aura and migraine headache are parallel or sequential processes. Here, we show that a single spreading depolarization wave triggered from the primary visual cortex is powerful enough to elicit progressive, sustained increases of hemodynamic and sensory responses to percutaneous periorbital noxious stimuli recorded in S1 and insular ophthalmic fields. Sensitization of cortical ophthalmic fields by SD was bilateral, occurred with precise spatiotemporal profiles, and was significantly reduced by pretreatment with an NMDA antagonist. Combined high-resolution assessing of neurovascular coupling and electrophysiological activities has revealed a useful preclinical tool for deciphering central sensitization mechanisms involved in migraine attacks.

Received Sep. 8, 2021; revised June 14, 2022; accepted June 23, 2022.

Author contributions: L.V. designed research; L.B.-R., L.B., and L.V. performed research; M.T. and T.D. contributed unpublished reagents/analytic tools; L.B.-R., L.B., J.-C.M., M.T., T.D., Z.L., and L.V. analyzed data; and L.B.-R. and L.V. wrote the paper.

This work was supported by the Institut National de la Santé et de la Recherche Médicale, Université de Paris, and the Leducq Foundation (Grant 501100001674).

The authors declare no competing financial interests.

Correspondence should be addressed to Luis Villanueva at luis.villanueva@inserm.fr.

https://doi.org/10.1523/JNEUROSCI.1825-21.2022

Introduction

Although the exact pathogenesis of migraine remains to be determined, several clinical neurophysiological studies suggest the existence of a hyperexcitable state characterized by abnormal cortical processing that can be detected interictally (Aurora and Wilkinson, 2007; Coppola et al., 2007). Spreading depolarization, also known as cortical spreading depression, has been proposed as the pathophysiological substrate of migraine aura and as a possible endogenous trigger of headache pain (Charles and Baca,

2013; Noseda and Burstein, 2013; Dreier and Reiffurth, 2015; Brennan and Pietrobon, 2018). Spreading depolarization, which in animals can be induced by focal stimulation of the cerebral cortex, is a slowly propagating wave of neuronal depolarization and glial activation (Piilgaard and Lauritzen, 2009; Dreier and Reiffurth, 2015; Parker et al., 2021). Early functional imaging studies during migraine attacks showed a propagation of cortical oligemia followed by hyperemia, involving widespread areas of the cortex (Olesen et al., 1990; Woods et al., 1994). Also, a temporal correlation has been observed between changes in blood oxygenation level-dependent (BOLD) signals of the occipital cortex and the aura perception (Hadjikhani et al., 2001). These studies strongly suggest a neurovascular link between migraine aura and SD, but its influence on migraine headache triggering remains unclear.

Animal studies suggest that SD waves trigger bottom-up mechanisms by the release of pro-inflammatory mediators, enhancing meningeal nociceptors excitability following local neurogenic inflammation (Bolay et al., 2002; Zhang et al., 2010). SD also regulates the activities of medullary trigeminovascular neurons that convey messages to thalamocortical areas involved in headache processing via top-down descending cortico-trigeminal modulation originating in primary somatosensory (S1) and insular (INS) cortex (Noseda et al., 2010). S1 and INS cortices are major targets of medullary trigemino-thalamic nociceptive afferents (Noseda et al., 2008; Vierck et al., 2013; Craig, 2014) and have been involved in migraine attacks (Borsook et al., 2016; Youssef et al., 2017; Jia et al., 2020). However, the precise role of peripheral versus central sensitization mechanisms in migraine headache processing remains to be determined.

Here, we examined simultaneously the impact of SD on bottom-up and top-down craniofacial trigeminal processing by assessing hemodynamic and synaptic mechanisms at the S1 and INS levels. For this, we used *in vivo* functional ultrasound (fUS) imaging of relative cerebral blood volume (rCBV) with high spatial and temporal resolution (Deffieux et al., 2018) for detection of transient hemodynamic changes in the brain (Macé et al., 2011; Sieu et al., 2015; Boido et al., 2019). We paired these neurovascular changes with local field potential (LFP) recordings to evaluate cortical excitability within the ophthalmic trigeminal field of S1 while percutaneous calibrated stimulation is applied in its peripheral receptive field (contralateral periorbital region). We found an NMDA-dependent mechanism linking SD-induced changes of rCBV and electrophysiological markers of cortical excitability. These findings may contribute to understanding the role of central sensitization mechanisms in migraine headache triggering.

Materials and Methods

Experimental design

Adult male Sprague Dawley rats (Janvier Labs) weighing 200–350 g were used in this study. All protocols were approved by our animal ethics committee at Paris V University (Authorization of Projects Using Animals for Research 24492 No. 202004211454660 v1), conducted in accordance with directives of the International Association for the Study of Pain (Zimmermann, 1983).

Rats were anesthetized with 3% isoflurane (Vetflurane, 1 × g/ml solution; Virbac) mixed in a vaporizer with 100% room air delivered at 0.5 l/min. Once the animals were deeply anesthetized, cannulas were inserted into the trachea and a jugular vein. After the animals were intubated, 2% isoflurane in 100% room air was delivered at a rate of 100 ml/min. Rats were paralyzed by intravenous injection of gallamine triethiodide (10 mg/h; Sigma-Aldrich) and artificially ventilated at a rate of 52 strokes/min. A normal acid-base equilibrium, respiratory frequency, end-tidal, inspired, and expired CO_2, O_2, and isoflurane levels were monitored and maintained using a compact monitor (Datex-Ohmeda, GE Healthcare) through a catheter inserted in the trachea. A heating blanket was placed under the animal during surgery to maintain the body temperature at 37°C (ATC1000 Temperature Controller, World Precision Instruments). Each animal was fixed in a stereotaxic frame, the head was shaved and then the scalp removed over the entire dorsal skull. The skin was trimmed laterally, and the temporal muscles were gently detached from the bone on both sides of the skull. For coronal imaging, a bilateral thinned skull was performed over the S1/INS cortex region (bregma −2.00 to −4.00 mm and ±5.00 mm lateral to the midline) according to Paxinos atlas coordinates (Paxinos and Watson, 1998) using a low-speed dental drill and a 1.4 mm burr (Fig. 1). For sagittal imaging, only the right hemisphere bone was removed from bregma +4.00 to −8.00 mm and laterally from 2.00 to 5.00 mm. To avoid overheating of the brain, cold Ringer lactate (CMD Lavoisier) was added continuously during the drilling sessions. A second 1.00-mm-diameter craniotomy was performed on the right lambdoid suture for KCl (1 M) topical application on the dura surface over the primary visual cortex (V1) region (bregma −9.00 mm, 3.00 mm lateral to the midline). Special attention was paid to avoid damaging the meninges.

Electrophysiological setup

Once the surgical procedures were finished, the level of anesthesia was lowered to 1.5% isoflurane. One hour after the end of the surgery, extracellular single units and LFPs were recorded using quartz-insulated, platinum tungsten microelectrodes, custom ground to impedances of 2–4 MΩ. Five electrodes were positioned 300 µm apart in the anteroposterior axis on the right S1 cortex (bregma −3.60 mm, 7.00 mm lateral to the midline with a coronal angle of 16°) and advanced independently using a five-channel Eckhorn mini matrix microdrive system to allow recordings in the somatosensory receptive fields over a large extent in the coronal plan (Thomas Recording). This device allows smooth movements performed with independently adjustable electrodes that are quite thin (60 µm shaft, 10 µm tip diameter) but strong enough to penetrate the dura, thus reducing the damage to the neural tissue (Eckhorn and Thomas, 1993). Once S1 neurons driven by periorbital receptive fields were identified, a layer of 2% Ringer's lactate-agarose was applied to cover the coronal or sagittal craniotomy. Microelectrode signals were amplified, digitized, and notch filtered. Raw electrophysiological signals were played through an audio speaker, displayed on an oscilloscope for additional inspection and recorded with Spike 2 software (version 7, Cambridge Electronic Design). Waveforms were stored on a computer for off-line analysis.

fUS imaging procedure

The fUS imaging was performed using a custom 15 MHz ultrasonic probe prototype (15 MHz, 128 elements, 0.110 mm pitch, Vermon) connected to an ultrafast research ultrasound scanner (128 channels, 62.5 MHz sampling rate) with real-time Neuroscan neuroimaging software (Technological and Research Accelerator in Biomedical Ultrasound, Institut National de la Santé et de la Recherche Médicale U1273 and Iconeus). The prototype implements real-time transcranial functional ultrasound imaging. Briefly, each single CBV image was obtained from recording 200 compounded ultrasonic frames acquired at a 500 Hz frame rate, each frame consisting of the coherent summation of backscattered echos from 11 tilted plane wave transmissions separated by a 2° angle (−10, −8,−6,−4,−2, 0, 2, 4, 6, 8, 10°) acquired at a 5500 Hz pulse repetition frequency. Imaging sessions were performed by real-time continuous acquisitions of successive blocks of 400 ms of compounded plane wave imaging with no dead time. Each block was processed using a SVD spatiotemporal clutter filter (Demené et al., 2015) to separate tissue from blood flow signals using a cutoff value of 60 and then time averaged to obtain a new power Doppler image. The combination of ultrafast imaging, coherent compounding, and spatiotemporal clutter filtering allows high spatial (less than 100 µm × 100 µm in the imaging plane, slice thickness of 400 µm, penetration depth >2 cm)

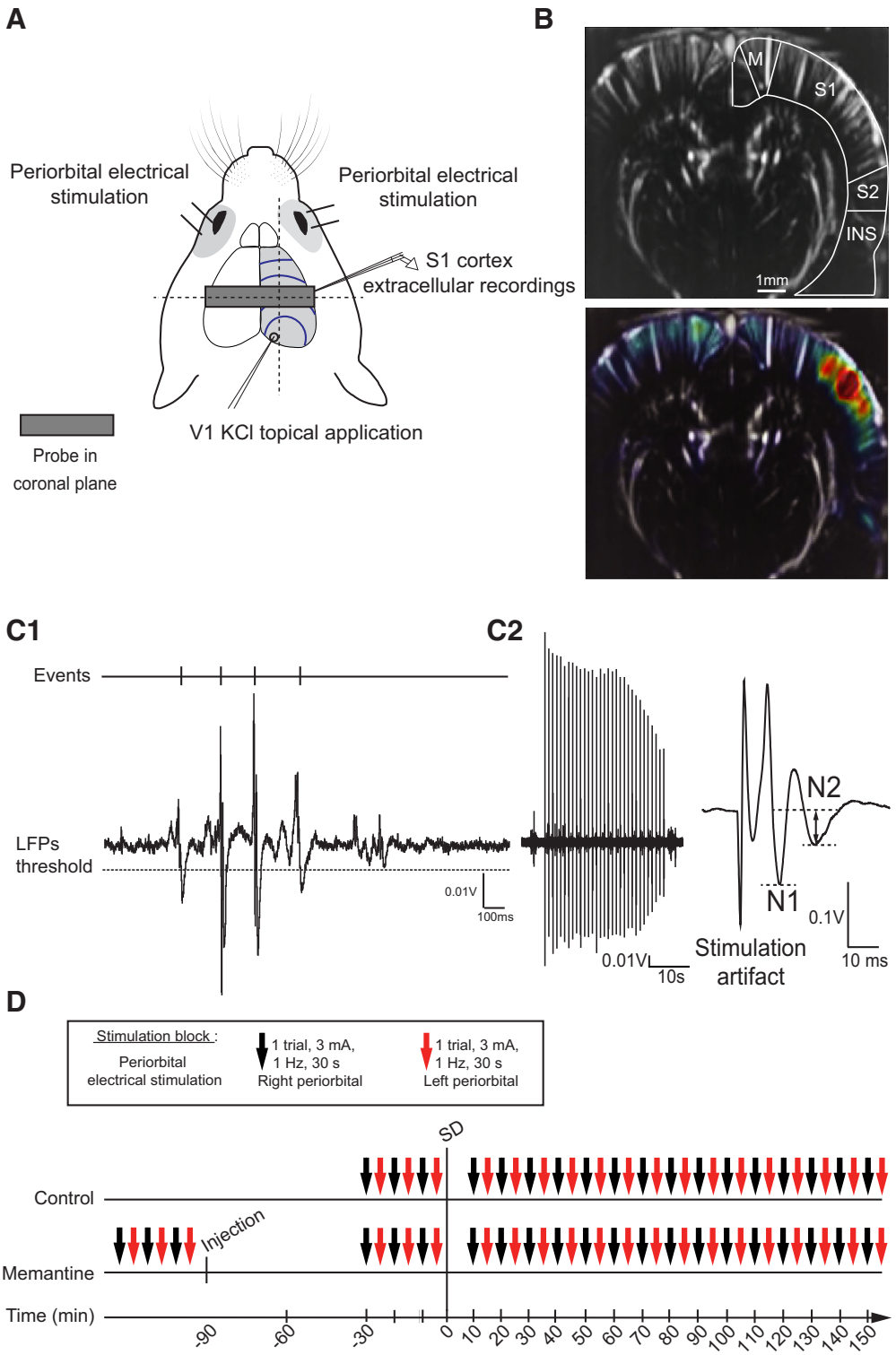

Figure 1. Experimental setup. ***A***, Simultaneous coronal plane fUS and LFP recordings of right S1 cortex ophthalmic fields. A small 1-mm-diameter craniotomy was performed above the right V1 cortex for triggering SD by a topical application of 1 M KCl. Repetitive (1 Hz) periorbital percutaneous electrical stimuli (30 single 3 mA, 1 ms square pulses) were delivered on the right or left receptive fields. ***B***, Coronal plane fUS images at bregma −3.6 mm, showing cortical microvasculature and imaging during left periorbital stimulation. ***C1***, Example of conversion of spontaneous LFPs to single events; the dashed line represents the LFP amplitude thresholding set to >5 SDs from baseline. ***C2***, Single and average examples of SEPs evoked by repetitive periorbital stimulations. SEP amplitude changes were measured on the N2 phase as the voltage difference between the two dashed lines. ***D***, Experimental design for assessments of rCBV and SEP responses. M, Motor.

and temporal (start at ~0.3 s and peak at ~1 s in response to ultrashort 300 µs stimuli) resolution imaging of CBV changes measured with fUS (Macé et al., 2011; Deffieux et al., 2018; Boido et al., 2019). fUS images were acquired at 1 Hz during electrical stimulation periods, whereas a frequency of 2.5 Hz was used during SD acquisitions. All images were processed online and stored on a computer for offline analyses.

The ultrasound probe was mounted on four motors (three translation plus one rotation, Physik Instrumente) for easy positioning and was oriented either in coronal or sagittal planes according

to the craniotomy. A layer of isotonic gel (Uni'Gel US, Aspet InMed) ensured acoustic coupling between the probe and the brain. Rats were imaged without contrast agents on an antivibratory table (TMC).

Single SD wave induction

SD was induced by a topical application of 50 µl of 1 M KCl on the dura over the right V1 cortex. KCl was cleaned and washed with Ringer's lactate 30 s after detection of the first electrophysiological burst triggered by SD. We confirmed previous findings (Parker et al., 2021) showing that in all our experiments, this procedure elicits only a single SD wave. No systematic *in vivo* studies of diffusion mechanisms following topical meningeal application of KCl have been reported. However, because the dural membrane is not primarily a lipid barrier, relevant mechanisms involve probably a concentration gradient diffusion process. This is supported by our early trials showing the triggering of multiple spreading depolarization waves (~5 up to 10 spreading waves in a 90 min period) when the KCl solution was left over the dura without washout. It could be assumed that in addition to its molecular shape, lipophilicity, and degree of ionization, the transdural transfer of KCl is due mainly to diffusion gradients, with a strong, early impact on superficial cortical layers. Moreover, control experiments using the topical application of saline on the dura over the V1 cortex showed a lack of effects on both baseline periorbital-evoked hemodynamic and synaptic activities over a 90 min period after saline application.

Percutaneous periorbital stimulation and rCBV images acquisition

A first search of cell clusters responding to tactile stimulation of the ophthalmic dermatome of the trigeminal nerve was performed. Once these clusters were encountered, a systematic search was performed for neurons responding to electrical stimulation through a constant current generator (DS3, Digitimer) using two needle electrodes inserted under the periorbital skin. Once a cell cluster responding to periorbital stimuli was found, a 10–20 min resting period was left, allowing the neurons to return to their steady-state baseline activity. This protocol is suitable for accurate measurements of control baseline activities.

For combined fUS imaging and electrophysiological data recordings (Fig. 1), each trial consisted of a 30 s prestimulus baseline recording period followed by a 30 s percutaneous, periorbital stimulation period (1 ms square pulse width, 1 Hz) and finally a poststimulus fUS period of 30 s, resulting in a total duration of 90 s. A 5 min recovery period was left after each trial. Three trials of control responses at 3 mA intensity were obtained before cortical application of KCl. Post-SD tests of left- and right-side periorbital stimulation of cutaneous receptive fields at different time windows were applied during a 150 min period as shown in Figure 1*D*.

LFPs, somatosensory evoked potentials, and rCBV signals, off-line analysis

Electrophysiology. Raw data were downsampled at 1 kHz, bandpass filtered at 0.1–120 Hz with Spike 2 software for specific LFP analyses. This bandpass was chosen based on the literature showing that hemodynamic signals are more strongly coupled to LFP activities than to firing rates (Mathiesen et al., 2000; Logothetis et al., 2001; Lauritzen et al., 2012). LFPs do not reflect the action potentials carried by the output neurons but rather varied aspects of the input signal within the recorded area. As reviewed by Logothetis and Wandell (2004) LFPs reflect primarily a weighted average of synchronized dendrosomatic components of the synaptic signals of a neuronal population, including after potentials and voltage-gated membrane oscillations. At the cortical level, LFPs include local intracortical processing mediated by the subthreshold signals of interneurons. In general, as also observed under our experimental conditions, LFPs and multiunit activities vary in a similar manner; hence, at those sites where LFPs predict the BOLD response, the multiunit does too. This is likely to be the case in most studies of bottom-up sensory processing where both afferent and efferent activity increase proportionally (Logothetis and Wandell, 2004). However, even in such cases there is a tendency for the LFP-based estimate to perform better than the multiunit. Also, the best match of LFPs and hemodynamic signals during visual processing has been found in the gamma frequency range of the LFPs (Kayser et al., 2004; Niessing et al., 2005).

A direct validation of neurovascular coupling under similar experimental conditions as the present work has been shown by Urban et al. (2014). fUS was revealed to be sensitive enough to detect hemodynamic and neuronal responses in S1 evoked only by a single pulse of percutaneous electrical stimulation applied on the hindpaw. Moreover, when measuring the rCBV response function following repetitive percutaneous electrical stimuli, ranging from 1 (200 μs) to 25 pulses (5 s), rCBV parameters including the peak amplitude, time-to-peak, full-width at half-maximum, and the spatial extent of the activated area are confined to S1 hindpaw representation, which increases with stimulus duration. Important also, ΣLFPs (the sum of LFPs), representing the product of LFP amplitude response, was proportional to the number of pulses, as expected from the literature.

Other proofs of concept of the usefulness of assessing neurovascular coupling using simultaneous EEG and fUS recordings was reported by Sieu et al. (2015) in awake mobile rats. They found a high spatiotemporal resolution/correlation between fUS and electrophysiological cerebral hemodynamics in a behavioral study on theta rhythm activation in a maze running task and a disease-related study on spontaneous epileptic seizures. More recently, Provansal et al. (2021) showed the possibility to detect deep optogenetic activations in anesthetized rats expressing the red-shifted opsin ChrimsonR in V1 cortex using fUS imaging. They demonstrate the optogenetic specificity of these activations and their neuronal origin with electrophysiological recordings.

As illustrated in the individual examples of spontaneous LFP recordings in Figure 2, *A1–A2*, thresholding of spontaneous LFP amplitude changes to >5 SDs was set for detecting changes in cortical baseline activity. This activity was counted during 60 s recording periods at different times after KCl infusion. The negative peak frequency was normalized with regard to the background activity values calculated from a 60 s period before KCl application.

As shown in Figures 1*C2* and 2*B*, somatosensory evoked potential (SEP) changes evoked by repetitive periorbital stimuli were measured on the N2 phase as the voltage difference between two dashed lines. SEP amplitude was calculated as the difference between the negative peak and baseline. As control, three trials of 30 s electrical stimulation were applied with the same intensity and then averaged. Post-SD tests were also averaged the same way for each stimulation time. This resulted in single averaged SEP data at each stimulation time in each animal. The sum of SEPs (ΣSEPs) was then calculated as the product of SEPs amplitude (mV) and the stimulus rate (Hz; Masamoto et al., 2007). The ΣSEPs values are expressed regarding the mean values obtained on control stimulation sequences, this mean representing 100%.

rCBV signal processing

The rCBV signal was extracted from a 370 pixel regions of interest (ROIs) in right S1, INS, and left S1 and averaged. Because the ultrasonic probe prototype was not large enough to include the whole left hemisphere, it was impossible to record rCBV signals from the left INS. For each animal, ROIs were manually defined according to the most periorbital-activated voxels in the right S1, INS cortices, and left S1 cortex. The area under curve (AUC) was calculated for rCBV signals during the baseline and the stimulation periods (30–60s) for each stimulation time (pre- and post-SD). The AUC values were normalized to the baseline level. For rCBV responses to periorbital stimulation, the baseline corresponded to the 30 s period before electrical stimulation. For the SD imaging, the baseline corresponded to the 30 s period before KCl application.

Pharmacological treatments

We tested the effects of the intravenous injection of the NMDA antagonist Memantine ($n = 6$) 15 mg/kg in 's lactate, Sigma-Aldrich). To assess the effects of SD induced by KCl, periorbital stimuli were applied before injection, then 1 h after injection, and during 150 min after SD (Fig. 1*D*).

Statistical analysis

For LFP and rCBV studies, statistical analyses were performed using Prism 8 software (GraphPad). Evoked SEP amplitude and spontaneous

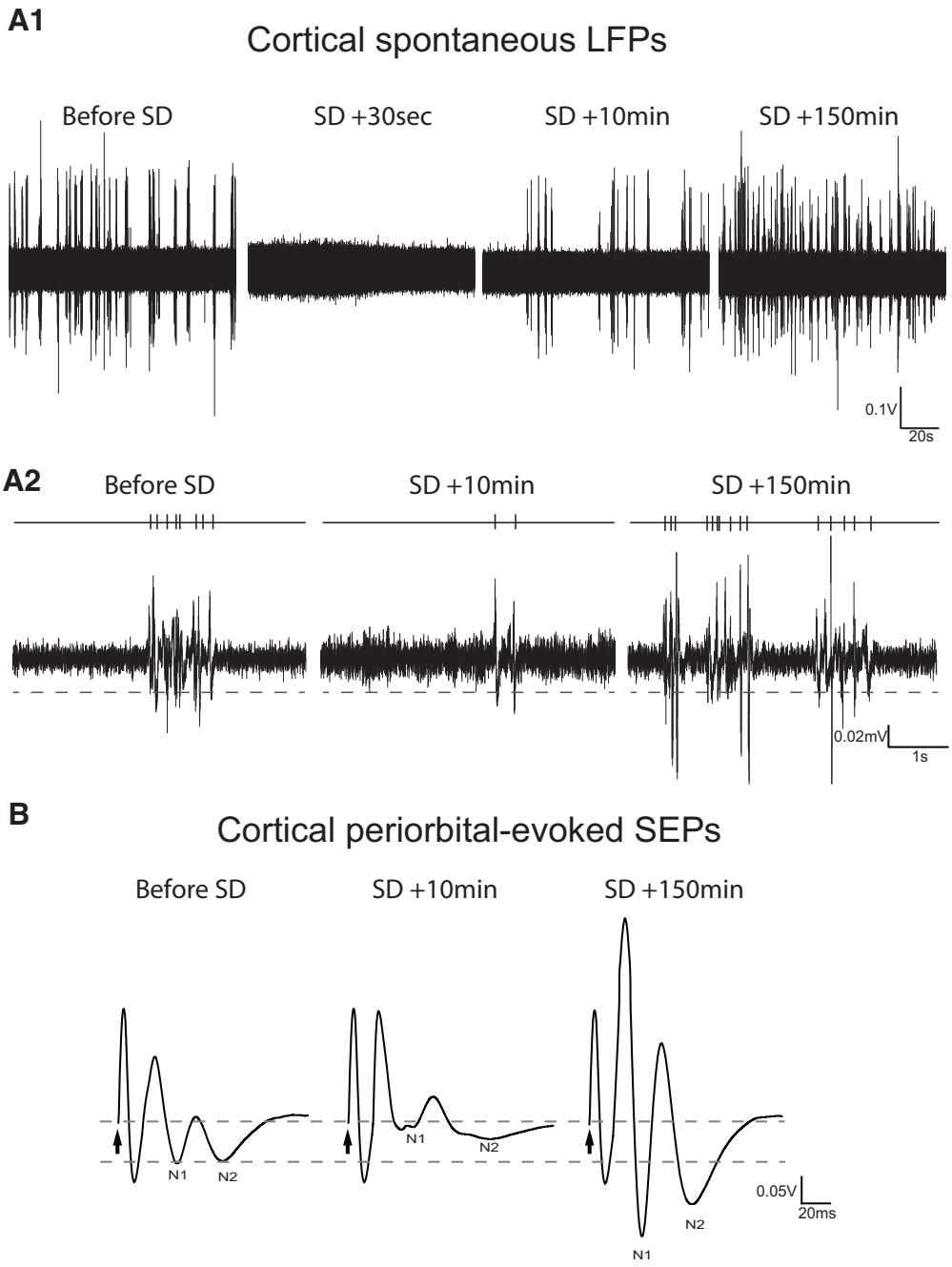

Figure 2. Individual examples of spontaneous LFPs and periorbital-evoked SEP local field potentials recorded in the right S1 cortex before and after SD triggered in the ipsilateral V1 cortex. ***A1***, S1 LFP activities before and after SD. ***A2***, S1 LFPs shown in expanded time scale. ***B***, Single periorbital-evoked (arrows) S1 SEPs before and 10 and 150 min after SD.

LFP negative peak frequency cumulative data are expressed as the mean ± SEM of the percentage changes of the mean values obtained before SD induction. A D'Agostino–Pearson normality test (omnibus K2) was performed for each dataset. Analyses were performed by comparing pre- and post-SD scores using one-way ANOVA with repeated measures based on a two-factor general linear model (GLM).

A two-way ANOVA with repeated measures based on the GLM followed by Sidak's multiple comparisons test were used for comparisons between drug treatments. One-way ANOVA with repeated measures based on the two-factor GLM followed by Dunnett's multiple comparisons test was performed to determine significance in ΣLFPs between control and over a 150 min post-SD period in saline control rats. Statistical significance was defined as $p < 0.05$.

For rCBV signal analyses, cumulative AUCs of rCBV data were expressed as the mean ± SEM of the percentage changes with regard to the mean baseline values obtained during the control time. A D'Agostino–Pearson normality test (omnibus K2) was performed for each dataset. To assess variation of rCBV baseline or rCBV responses to periorbital stimulations within the same group, a one-way ANOVA with repeated measures based on a two-factor GLM was applied in case of normal distribution, and a one-way ANOVA with repeated measures based on a Friedman test was applied in case of non-normal distribution. One-way ANOVA test was followed by a Dunn's or a Dunnett's multiple comparisons test.

Two-way ANOVA with repeated measures based on GLM followed by a Sidak's multiple comparisons test were performed to compare baseline activities and activation after contralateral periorbital stimulation before and after SD between right S1 and left S1 cortices and right S1 and right insular cortices. Finally, comparisons of rCBV signals induced by SD between nontreated and treated groups were conducted with a

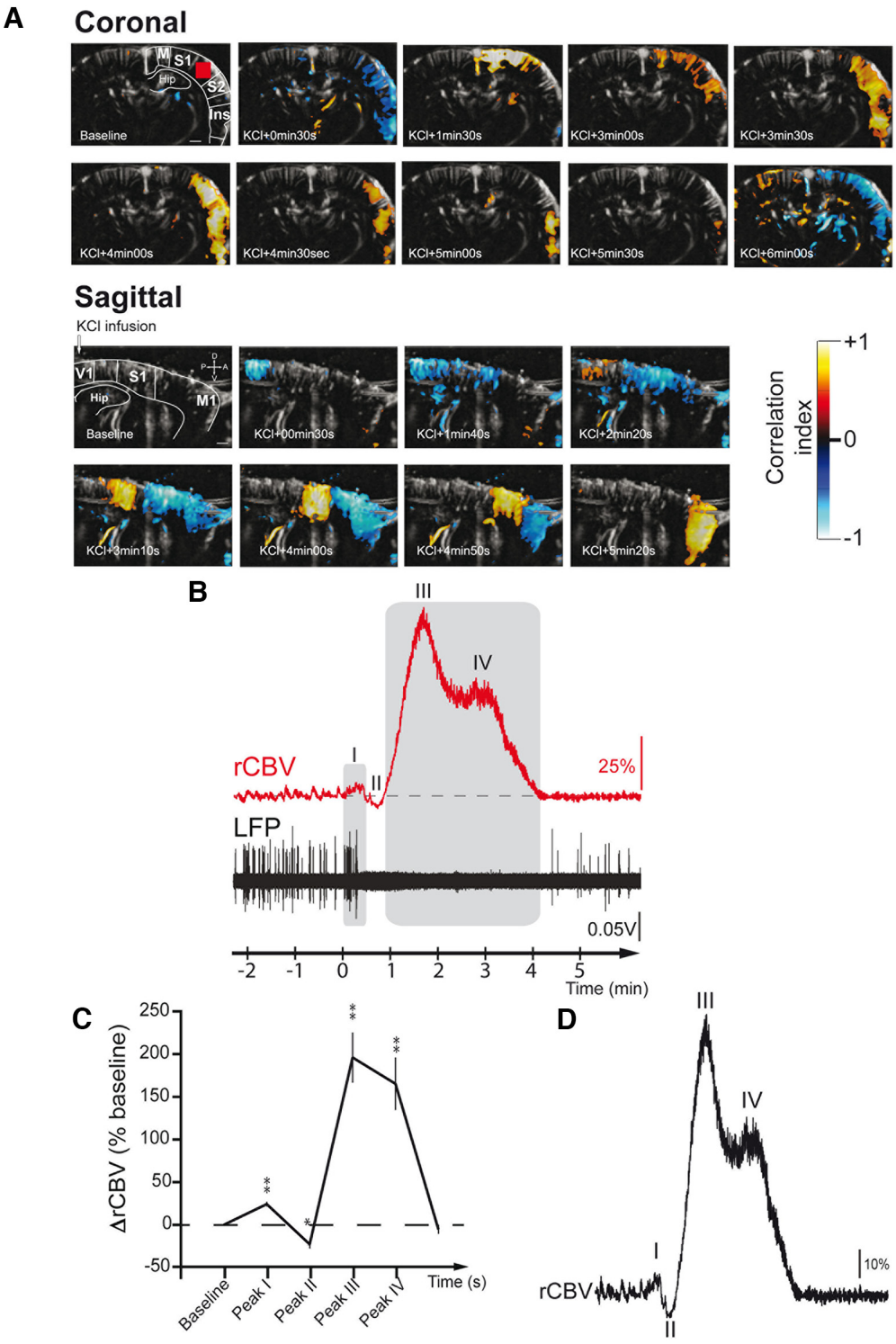

Figure 3. Spatiotemporal hemodynamic and neuronal activities observed following a single SD wave elicited by KCl application in the V1 cortex. ***A***, Frames extracted at different time points from fUS imaging movies depicting rCBV changes elicited by a spreading depolarization triggered in V1 cortex. Sagittal and coronal views showed a quadriphasic wave with consecutive increases (yellow) and decreases (blue) of rCBV during 6 min. Probes were placed in either coronal or sagittal planes. Hip, Hippocampus; M, motor. ***B***, time course of the rCBV (red plot) and neuronal activity (LFPs, black plot) recorded in S1 during a spreading depolarization. The red box in the coronal μDoppler image in ***A*** represents the ROI from where the rCBV signal was extracted. Initial rCBV increases (phase I) were correlated with a strong neuronal burst followed by a brief hypoperfusion (phase II) associated with the starting of a long-lasting complete neuronal depression. SD then elicited a strong increase in rCBV (phase III) followed by a plateau (phase IV). The rCBV recovery was followed by a slow recovery of neuronal activity. ***C***, Cumulative results showing the detailed quadriphasic rCBV profile of SD waves recorded in S1 ($n = 8$), expressed as mean ± SEM of the percentage changes regarding the mean values obtained before KCl application. ***D***, Individual example showing a quadriphasic rCBV response triggered by SD.

two-way ANOVA with uncorrected Fisher's least significant difference. Statistical significance was defined as $p < 0.05$.

Results

SD originating from V1 cortex triggers neurovascular waves spreading in the cortical pain matrix

High spatiotemporal resolution images of the brain microvasculature with fUS imaging allowed us to assess the spatial spread of SD waves in lateral and sagittal directions, including S1 and INS (Fig. 3*A*).

As previously observed (Dreier and Reiffurth, 2015; Sawant-Pokam et al., 2017; Parker et al., 2021) a calibrated, single SD originating within V1 causes a brief synaptic activation wave followed by a strong depression of basal activity (Fig. 3*B*). The neuronal SD is accompanied by a hemodynamic wave including four phases (I to IV) of rCBV increases and decreases that propagate in the ipsilateral hemisphere with a velocity of 4.0 ± 0.4 mm/min (n = 8), whose effects persisted during the whole 150 min post-SD period of imaging.

The propagation of SD from V1 elicited a brief, moderate increase of rCBV in S1 (+26.7 ± 5.3%) associated with a strong increase in the number of LFPs (664.4 + 81.8%), which may correspond to the strong depolarization spreading from posterior to anterior cortices (phase I; Fig. 3*B*). The initial increase was followed by a slight rCBV decrease (−18.2 ± 6.2%) of short duration associated with the depression (−68.2 ± 11.1%) of electrophysiological activities (phase II). Then, a massive rCBV increase (202.2 ± 46.9%) associated with a strong depression of electrophysiological activities (−74.1 ± 13.5% of control value) was observed in S1 (phase III; Fig. 3*B*,*C*,*D*). Finally, after the peak of neurovascular uncoupling observed in phase III, the progressive decreasing phase of rCBV was followed by a plateau (phase IV, 170.3 ± 32.8%) then a decay coincident with the starting of LFPs recovery.

The SD wave triggered from V1 propagated first to S1 and then spread to caudal INS regions. As shown by the mean latency values of phase III spread, it was found that compared with INS, phase III occurs at a significant shorter latency in S1(221 ± 22 s in S1 and 261 ± 37 s in INS). Compared with the right S1 cortex, the left S1 was not directly affected by SD during the 600 s that followed KCl application (600 s post-KCl, right S1 cortex, AUC, 18,770 ± 573.6 a.u.; left S1 cortex, AUC, 5147 ± 425.6 u.a., n = 12).

The rCBV basal signal increased progressively in S1 and INS regions containing the periorbital receptive fields (Fig. 4). Compared with the right hemisphere directly affected by SD, rCBV increases of lower magnitude were observed in the left S1 side (Fig. 4*A*). Increases of similar magnitude and time course were observed for rCBV and LFPs signals in the right S1 area (Fig. 4*B*). rCBV increases in INS were of lower magnitude but followed a similar time course compared with S1(Fig. 4*C*).

Control data obtained following a topical application of CSF (50 µl drop) on the dura mater over the V1 cortex showed no changes in both basal rCBV signal and spontaneous LFPs in S1 cortex during the 100 min that followed its application (+0.02 ± 0.01%, p = 0.18 and +14.1 ± 10%, p = 0.27 of presaline values, respectively; n = 5).

Sustained facilitation of periorbital-evoked hemodynamic and electrophysiological responses in cortical ophthalmic fields after triggering SD from V1 cortex

As shown by the individual example in Figure 5, periorbital stimulation applied on the left cutaneous receptive field (Fig. 5*C*) elicited concomitant increases of rCBV and SEP responses recorded in the right S1 that were strongly amplified following SD triggering in the ipsilateral right V1 cortex. SD elicited progressive changes of rCBV and ΣSEPs in S1 and INS rCBV with precise spatiotemporal profiles (Fig. 6). SD induced an initial ipsilateral significant reduction of periorbital-evoked rCBV and ΣSEPs in S1 (Fig. 6*C*) and periorbital-evoked rCBV in INS (Fig.

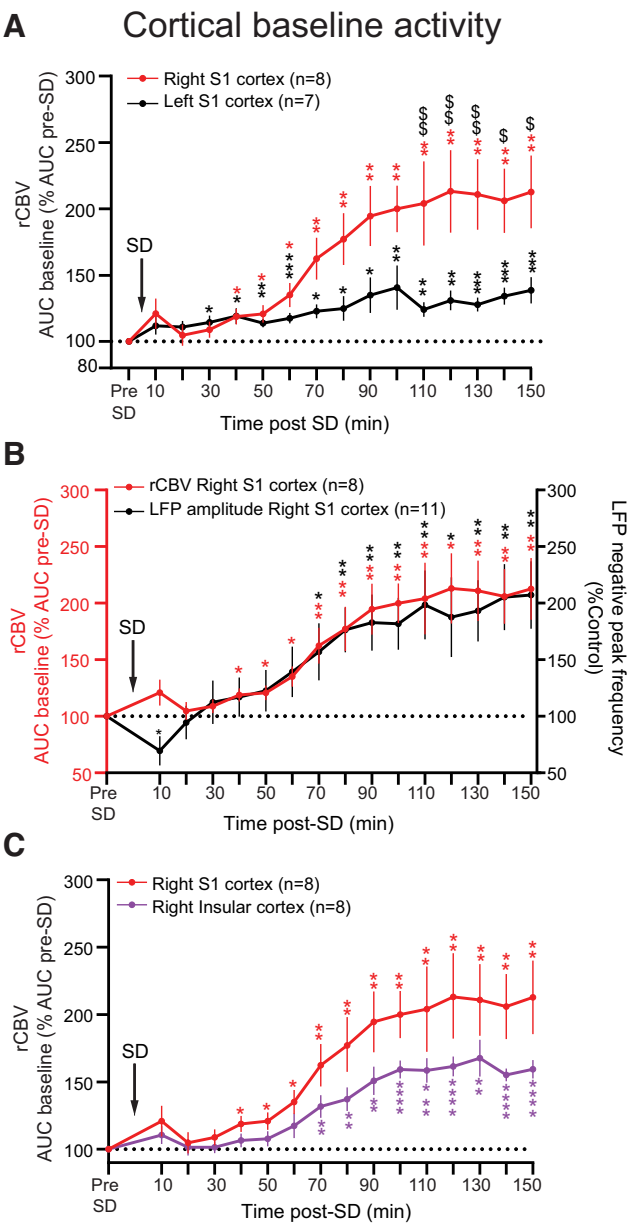

Figure 4. Spatiotemporal hemodynamic and neuronal basal activities following a single SD elicited in the right V1 cortex. Time course of the basal rCBV in the S1 and INS cortices ipsilateral (right) and contralateral (left) to the SD focus, before and 10–150 min after SD. ***A***, SD significatively increased the basal rCBV in both ipsilateral and contralateral S1 cortices. ***B***, Basal rCBV changes (red plot) and spontaneous LFP negative peak frequency (black plot) recorded in the ipsilateral S1 before and 10–150 min after SD. ***C***, Time course of the basal rCBV in the ipsilateral S1 (red plot) S1 and insular (purple plot) cortices before and 10–150 min after SD. SD significantly increased the basal rCBV in all cortices. Basal rCBV and spontaneous LFPs negative peak frequency data are expressed as mean ± SEM of the percentage changes regarding the mean value obtained before KCl infusion (*, $p < 0.05; **, $$p < 0.01; ***$p < 0.001, ****$p < 0.0001). Asterisks indicate statistical significance between the before and after SD values. Dollar signs indicate statistical significance between S1 or S1 and INS cortices.

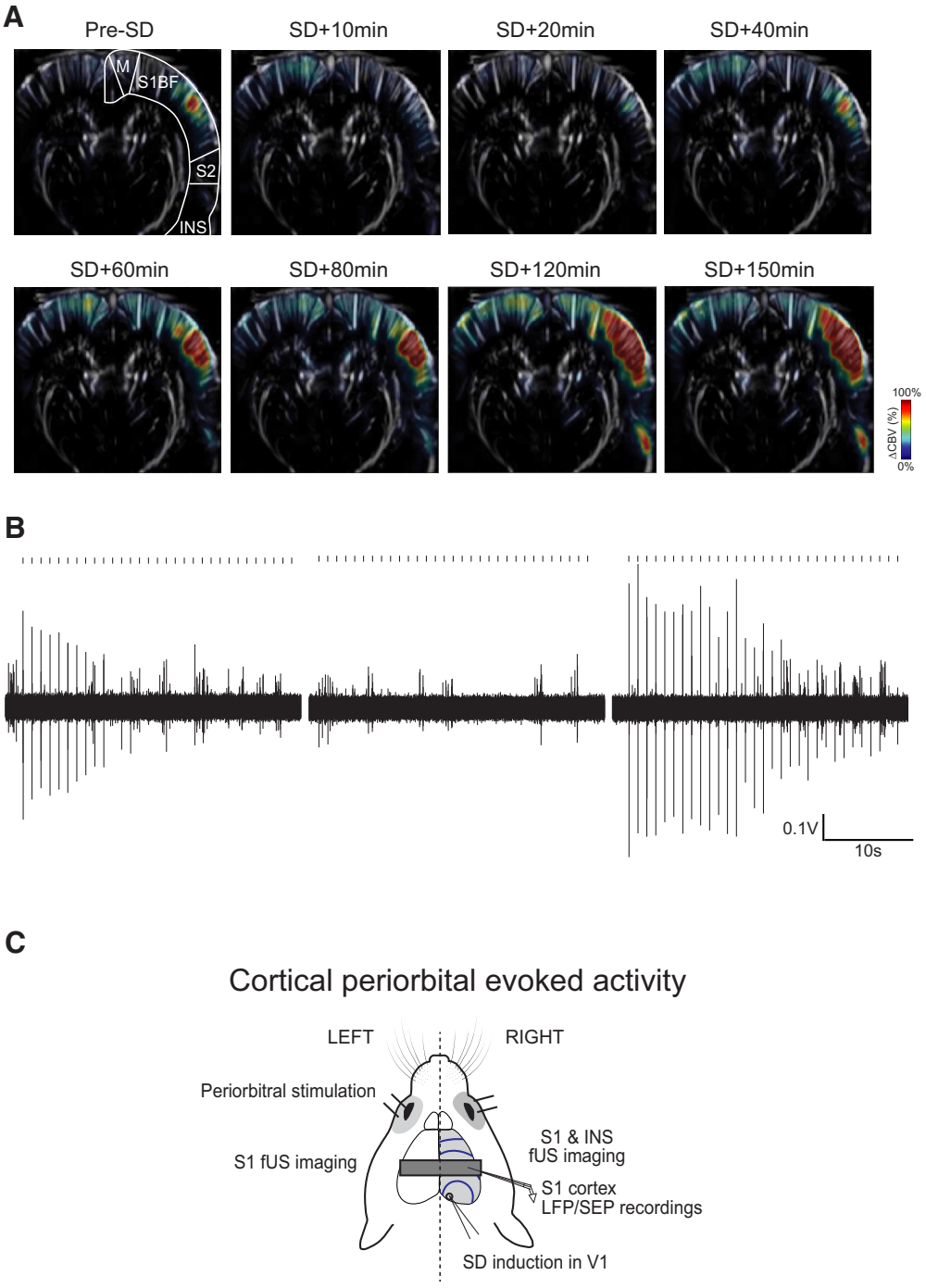

Figure 5. Individual example of the temporal evolution of rCBV and SEP responses evoked by 3 mA repetitive percutaneous periorbital stimulations applied on the left side, before and after SD. ***A***, Percutaneous periorbital stimuli elicited rCBV responses spatially restricted to the contralateral S1 and INS cortices before (pre-SD) and between 10 and 150 min after SD. ***B***, Corresponding SEP recordings in S1 ophthalmic fields of periorbital-evoked responses before and 10 and 150 min after SD. ***C***, Experimental setup.

6*D*). Periorbital-evoked S1 and INS rCBV increases reaching values similar to those of controls were observed 40 min after SD, then were significantly facilitated at 70 min, reaching their maximum at 130 min (S1, 290 ± 34.6%, $*p < 0.001$; INS, 254.8 ± 58.9%, $*p = 0.03$; $n = 8$) and remaining facilitated until the end of the 150 min imaging period. S1 periorbital-evoked ΣSEPs were also significantly decreased during the first 30 min following SD, with a pronounced drop observed ~10 min (60 ± 7% of control value, $F_{(2.725,29.98)} = 5{,}69$, $p \leq 0.01$; $n = 11$). This large decrease was followed by a progressive recovery of evoked ΣSEPs, reaching baseline levels ~30 min after SD (Fig. 6*C*). The ΣSEPs evoked by periorbital stimuli were facilitated at 70 min (141.9 ± 18.6%, $F_{(2.725,29.98)} = 5{,}69$, $p = 0.04$; $n = 11$) and remained facilitated until the end of the 150 min testing period.

In the opposite side of SD triggering (left S1), rCBV periorbital-evoked activities were initially unaffected by SD then were significantly facilitated (145.9 ± 14.7% of control value at 30 min post-SD, $p = 0.015$; $n = 7$) but at a significant lower magnitude compared with the SD triggering side (Fig. 6*B*).

Cumulative data obtained from a control CSF topical application (50 µl drop) on the dura mater over the V1 cortex showed no changes during 100 min recordings in both periorbital-

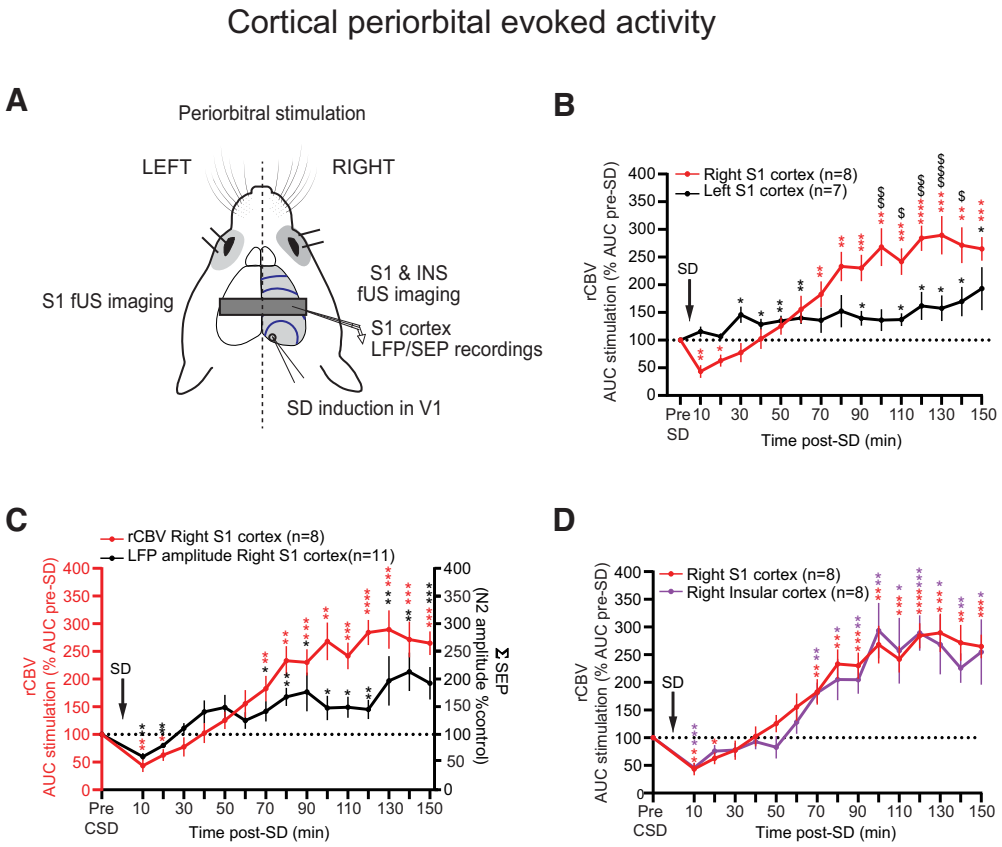

Figure 6. Spatiotemporal changes in hemodynamic and neuronal percutaneous periorbital-evoked activities following a single SD elicited in the right V1 cortex. ***A***, Schematic representation of the periorbital stimulation sites, fUS imaging, LFP, SEP recordings, and SD induction. ***B***, Time course of the periorbital-evoked rCBV in the ipsilateral (right, red plot) and contralateral (left, black plot) S1 cortices to the SD focus, before and 10–150 min after SD. ***C***, Periorbital-evoked rCBV (red plot) and ΣSEP amplitude (black plot) recorded in the right S1 before and 10–150 min after SD. ***D***, Time course of the periorbital-evoked rCBV in the right S1 (red plot) and INS (purple plot, $n = 8$) before and 10–150 min after SD. SD significatively increased the periorbital-evoked rCBV in both cortices. rCBV and SEP count data are expressed as mean ± SEM of the percentage changes with regard to the mean value obtained before KCl infusion (*, $p < 0.05$; **, $$p < 0.01$; ***, $$$p < 0.001$; ****$p<0.0001$). Asterisks indicate statistical significance between the before and after SD values. Dollar signs indicate statistical significance between S1 and INS cortices.

evoked rCBV and ΣSEP responses in S1 cortex (−0.8 ± 6.8%, $p = 0.9$ and +12 ± 8.1%, $p = 0.16$ of presaline values, respectively; $F_{(2.406,14.44)=1890}$; $n = 5$).

Cortical neurovascular activities following SD are modulated by an NMDA antagonist

Changes in S1 and INS activities associated with the spread of the SD wave originating in the ipsilateral right V1 cortex were compared with nontreated rats after systemic administration of the NMDA antagonist Memantine (Figs. 7, 8, 9).

Memantine did not affect the propagating speed of the SD wave (4.0 ± 0.2 mm/min pre-Memantine; 4.3 ± 0.4 mm/min post-Memantine, $p = 0.61$; $n = 5$) and phases I and III. In contrast, it blocked the hypoperfusion occurring during phase II and the plateau observed during phase IV (Fig. 7*A*,*B*).

Before SD induction, Memantine did not affect significantly S1 basal rCBV signals (60 min post-Memantine, right S1 cortex, −0.6 ± 8.5% of pre-Memantine values, $p = 0.95$, $F_{(1,5)} = 0{,}004$; $n = 6$). In contrast, Memantine significantly reduced basal LFPs activities recorded in S1 (−31,2 ± 9,5% of pre-Memantine values, $p = 0.02$, $F_{(1,5)} = 10.8$; $n = 6$).

Before SD induction, both spontaneous LFP- (Fig. 7*C1*) and rCBV periorbital-evoked responses (Fig. 7*C2*) were reduced by Memantine in S1 cortex (60 min post-Memantine; SEP, −48.8 ± 7.3% of pre-Memantine value, $p = 0.03$; rCBV, −30.7 ± 6.9% of pre-Memantine value, $p = 0.006$; $F_{(1,5)} = 20.99$; $n = 6$).

After SD induction, Memantine blocked SD-induced increases in basal rCBV in S1 and INS cortices (Fig. 8*A1*,*C1*) and SD-induced basal LFP increases in the right S1 (Fig. 8*A2*).

Changes elicited by SD in rCBV and SEP periorbital-evoked responses were compared in rats with and without Memantine administration.

A significant increase of S1 rCBV periorbital-evoked responses was observed 70 min after SD in nontreated rats, outlasting the whole 150 min recording period (Fig. 8*B1*). In Memantine-treated rats an increase of rCBV periorbital-evoked activity in the right S1 was observed 80 min after SD but occurred at significantly lower levels compared with control nontreated rats during the whole stimulation time (increases at 150 min post-SD, 264.8 ± 21.3% in nontreated rats, $n = 8$; 180.4 ± 23.5% in Memantine-treated rats, $p = 0.005$, $F_{(1,12)} = 10.92$, $n = 6$). In contrast, the increases in S1-evoked ΣSEPs elicited by periorbital stimulation after SD (Fig. 8*B2*) observed in nontreated rats were not reduced by Memantine administration (increases at 150 min after SD, 192.4 ± 29.6% in nontreated rats, $n = 11$; 231.6 ± 38.8% in Memantine-treated rats, $F_{(1,16)} = 0{,}06$, $p = 0.29$, $n = 6$). Before SD induction, Memantine did not affect significantly INS basal rCBV activities (60 min post-Memantine, −6.0 ± 5.3% of pre-Memantine values, $F_{(1,5)} = 1.3$, $p = 0.31$, $n = 6$). In contrast, Memantine significantly increased rCBV periorbital-evoked responses recorded in INS before SD induction (60 min post-Memantine, +92.6 ± 32.54% of pre-Memantine value, $p = 0.04$, $F_{(1,4)} = 8{,}1$, $n = 6$).

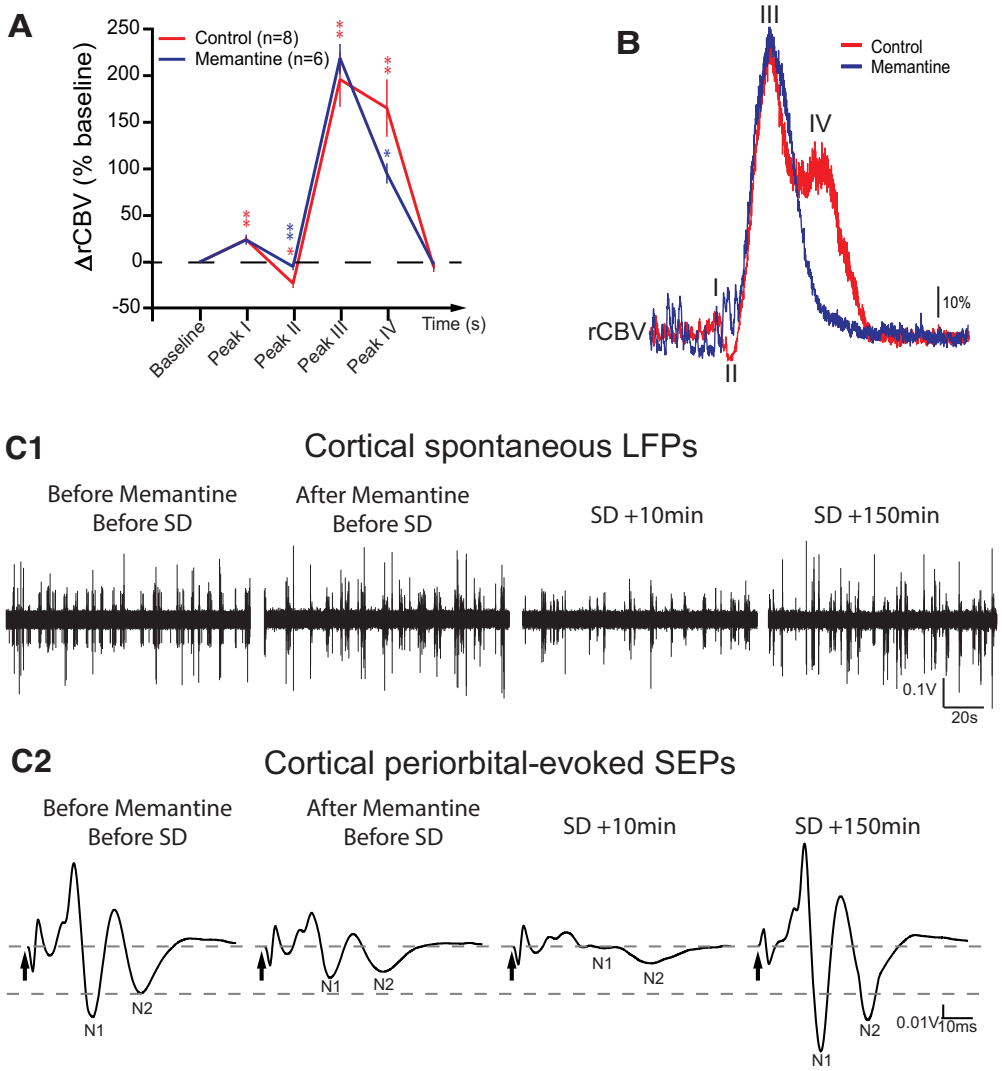

Figure 7. Memantine modulates cortical hemodynamic and neuronal activities. ***A***, Cumulative results showing the detailed quadriphasic rCBV profile of SD waves recorded in S1 in controls (red curve, $n = 8$) and rats pretreated with Memantine (blue curve, $n = 6$; expressed as mean ± SEM of the percentage changes regarding the mean values obtained before KCl application; $^{*}p < 0.05$, $^{**}p < 0.01$). ***B***, Individual examples showing a quadriphasic rCBV response in S1 triggered by SD in a control and a Memantine-treated rat. ***C1***, Individual examples of Memantine effects on spontaneous (LFP) and ***(C2)*** periorbital-evoked (SEP) local field potentials recorded in the right S1 cortex before and after spreading depolarization triggered in the ipsilateral V1 cortex.

The increase of INS rCBV basal responses by SD was abolished by Memantine injection (Fig. 8*C1*; 150 min after SD, +159.3 ± 7% of pre-SD value in nontreated rats, $n = 8$; +96.3 ± 7.7% of pre-SD value in Memantine-treated rats, $n = 6$; $p = 0.0003$, $F_{(1,192)} = 222.8$). The increase of INS rCBV periorbital-evoked responses in nontreated rats was also blocked by Memantine (150 min after SD, 254.8 ± 58.8% of pre-SD value in nontreated rats; 115 ± 24.6% of pre-SD value in Memantine-treated rats; $p = 0.001$, $F_{(1,12)} = 12.42$; Fig. 8*C2*).

In the left hemisphere (opposite to SD triggering; Fig. 9) before SD induction, Memantine administration did not modify S1 basal rCBV signal (60 min post-Memantine, −8.9 ± 9.75% of pre-Memantine value, $p = 0.40$, $F_{(1,5)} = 0{,}8$, $n = 6$) and significantly decreased the rCBV periorbital-evoked responses (60 min post-Memantine, −39.3 ± 12.8% of pre-Memantine value, $p = 0.04$, $F_{(1,4)} = 9.4$, $n = 6$). In contrast, Memantine blocked the basal rCBV activity increases in S1 elicited by SD (Fig. 9*A*). On the other hand, SD-evoked rCBV increases in periorbital-evoked activity in the left S1, opposite to SD triggering, were unaffected by Memantine administration (Fig. 9*B*).

Discussion

Sequential changes of hemodynamic and sensory cortical activities elicited by SD

Our findings show that a single SD wave originating in V1 triggers a cascade of time-locked hemodynamic and sensory changes affecting S1 and INS ophthalmic fields.

The quadriphasic time course and global profile of the early changes observed on cortical basal activities are similar to those reported in previous studies (Piilgaard and Lauritzen, 2009; Chang et al., 2010). Immediately after SD, it was possible to detect an early phase of neurovascular coupling in S1, consisting of concomitant increased LFPs and oligemia. Such post-SD oligemia is closely associated with changes in the capillary bed associated with constriction of pial capillaries as well as penetrating arteries (Anzabi et al., 2021). Similar rCBV decreases were detected before the large rCBV increase following SD in an fUS study (Rabut et al., 2019). Phases I and III were unaffected by the previous administration of the NMDA antagonist Memantine. In contrast, phases II and IV depend on NMDA-related activities as rCBV changes were blocked by Memantine, reducing the time

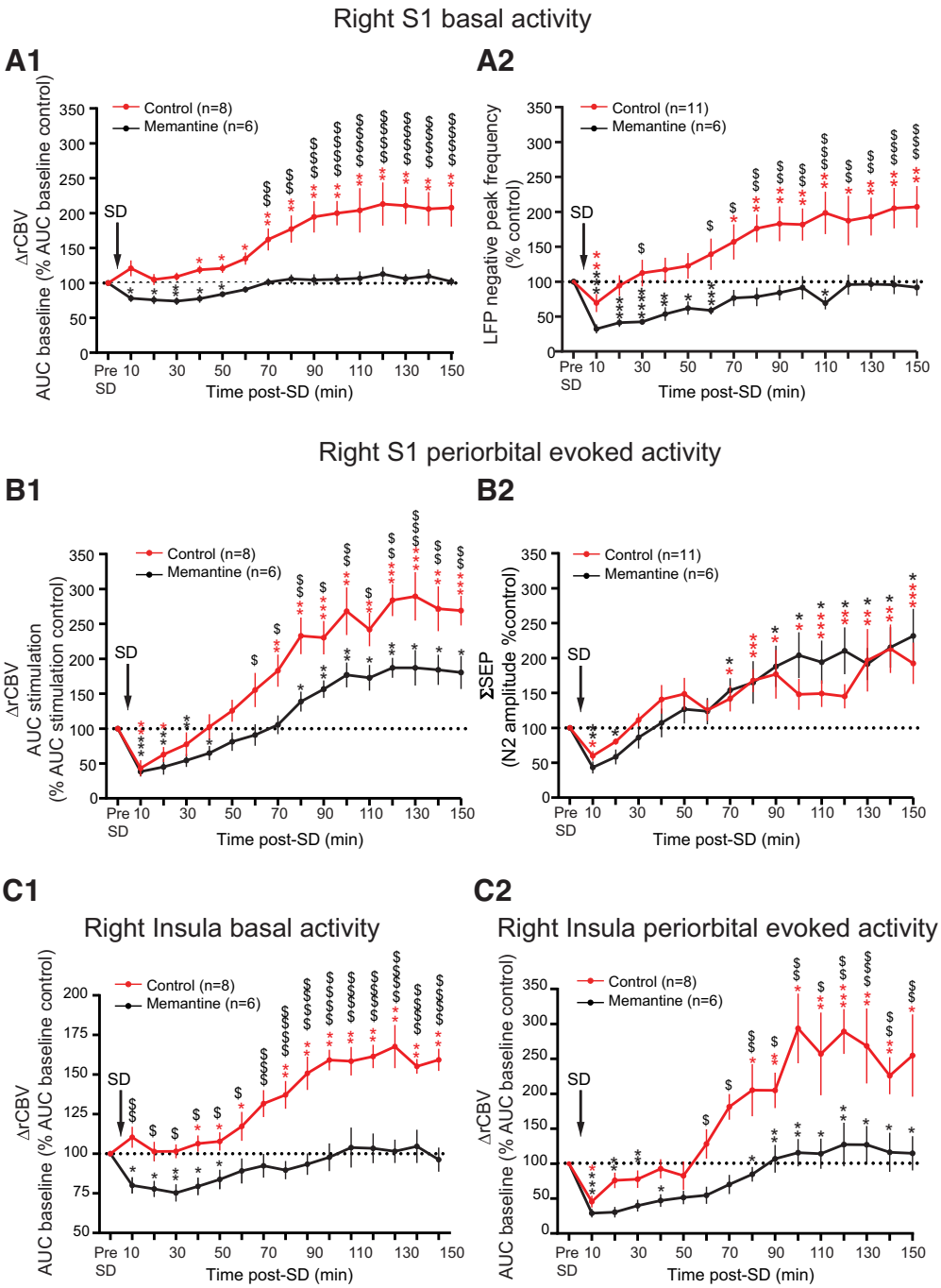

Figure 8. SD triggers spatiotemporal changes in hemodynamic and neuronal activities that are modulated by the intravenous injection of 15 mg/kg Memantine, an NMDA antagonist. ***A***, Basal rCBV (***A1***) and spontaneous LFP (***A2***) counts in S1 following an ipsilateral SD in controls (red plot) and pretreated rats with Memantine (black plot). Memantine significantly blocked the basal increases of hemodynamic and neuronal activities elicited by SD. ***B***, Periorbital-evoked rCBV (***B1***) and ΣSEP amplitudes (***B2***) in S1 following an ipsilateral SD in controls (red plot) and pretreated rats with Memantine (black plot). Memantine administration significantly decreased the periorbital-evoked hemodynamic response increases following SD but did not affect the neuronal evoked responses. ***C***, Basal (***C1***) and periorbital-evoked (***C2***) rCBV activities following a SD in ipsilateral V1 cortex in controls (red plot) and pretreated rats with Memantine (black plot). Memantine administration significantly blocked the periorbital-evoked increases of hemodynamic responses. rCBV data are expressed as mean ± SEM of the percentage changes with regard to the mean value obtained before KCl infusion (*, $$p < 0.05$$; **, $$\$p < 0.01$$; ***, $$\$\$\$p < 0.001$$; ****, $$\$\$\$\$p < 0.0001$$). Asterisks indicate statistical significance between the before and after SD values. Dollar signs indicate statistical significance between S1 and INS cortices.

for recovery from phase IV. Memantine was probably too weak to counteract the large rCBV increases observed in phase III because of its uncompetitive NMDA antagonist profile with moderate affinity, strong voltage dependency, and rapid unblocking kinetics (Parsons et al., 1999). It is also possible that the large CBV signals detected in phases III and IV are caused by a mixture of initial strong neuronal depolarization followed by glial activation, not depending only on glutamate signaling. The possibility to antagonize simultaneously, in a preventive fashion, metabolic and neuronal mechanisms triggered by SD is complex as our findings show that NMDA antagonist action on neurovascular versus electrophysiological responses is not always unidirectional. As suggested by previous studies, the early phase of strong depolarization and the

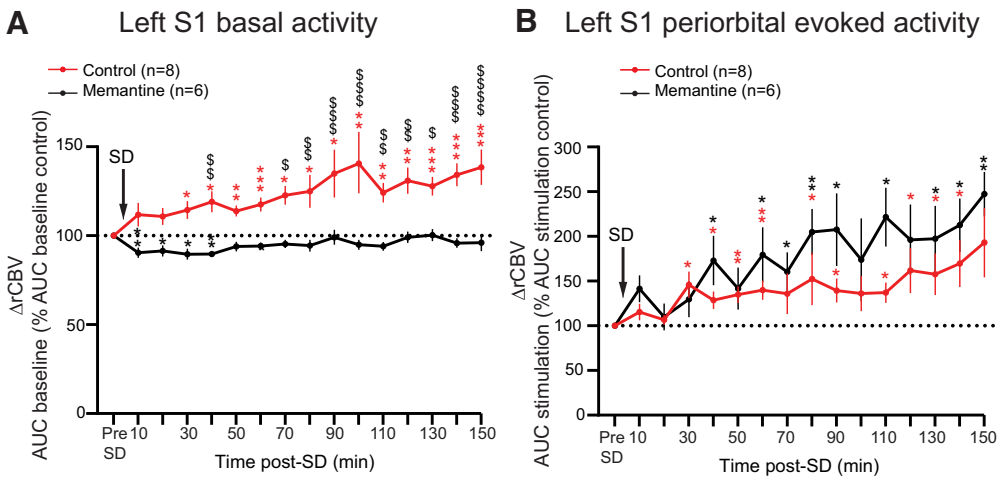

Figure 9. Spatiotemporal basal and periorbital-evoked hemodynamic activities in the left S1 cortex following a single SD wave elicited in the contralateral right V1 cortex are differentially modulated by Memantine. ***A***, Basal rCBV recorded in the left S1 cortex (red plot) following a contralateral (right) SD elicited in controls (red plot) and pretreated rats with Memantine (black plot). Memantine significantly blocked the basal increases of hemodynamic activities elicited by SD. ***B***, Increases of periorbital-evoked activity in the left S1 cortex by contralateral SD in controls (red plot) are unaffected by Memantine pretreatment (black plot). rCBV data are expressed as mean ± SEM of percentage changes with regard to the mean value obtained before KCl infusion (*, $p < 0.05$; **, $$p < 0.01$; ***, $$$p < 0.001$; ****, $$$$p < 0.0001). Asterisks indicate statistical significance between the before and after SD values. Dollar signs indicate statistical significance between S1 and INS cortices.

neuronal silence that follows are probably interdependent phenomena caused by excessive release of glutamate, involving complementary presynaptic and postsynaptic mechanisms (Sawant-Pokam et al., 2017). This results in strong local energy needs, as shown by the long-lasting increases observed in hemodynamic phases III and IV, probably resulting from astrocyte buffering action aimed at counteracting the dramatic changes in ionic gradients involved in excessive neuronal depolarizations at the origin of SD (Dreier and Reiffurth, 2015; Parker et al., 2020). Attempts to suppress SD by simultaneous NMDA and glial activity antagonism might thus produce the opposite action, namely, an increase of SD because of impaired clearance of glutamate by astrocytic blockade.

SD, cortical ophthalmic fields sensitization, and its possible relationship with migraine headache

A crucial question remains about how to establish a direct link between migraine, visual aura, and the resulting trigeminovascular dysfunction that generates headache pain. Our findings show that the sequential sensitization process underlying facilitation of cortical activities of the ipsilateral (right) hemisphere directly affected by SD differ from those observed in the opposite one. After SD, significantly larger increases in both the magnitude and progression of rCBV baseline activities occur in the right hemisphere, with similar time courses for increases in basal LFPs in S1 and rCBV in S1 and INS. An initial immediate reduction of S1 rCBV, SEP, and INS rCBV periorbital-evoked responses was only observed on the SD triggering side, probably mediated by a direct action of the SD wave. A 30 min recovery period was followed by a progressive facilitation of S1 ΣSEPs elicited by periorbital stimuli, with significant increases starting 70 min after SD. Interestingly, facilitation of periorbital rCBV-evoked responses starting on similar 70 min time frames was observed for both S1 and INS, suggesting a common, precise sequential process of central sensitization. According to the literature (Noseda and Burstein, 2013) this increased responsiveness could correspond to a late phase of nociceptive sensitization reaching third order thalamocortical neurons, relevant to the typical delay between the onset of visual aura, the onset of migraine headache, and the central sensitization that follows.

Rodent studies suggest that the hemisphere directly affected by SD triggers bottom-up signaling mechanisms via the release of pro-inflammatory mediators that activate and sensitize meningeal nociceptors (Bolay et al., 2002; Zhang et al., 2010), followed by a sensitization spread to cutaneous periorbital nociceptors, then medullary and thalamocortical neurons located in the opposite hemisphere (Noseda and Burstein, 2013). Such bottom-up mechanisms could mediate the enhanced basal and periorbital-evoked activity observed in the left S1 (contralateral to SD). Mirror-like transcallosal connections established between S1 and INS ophthalmic fields (Noseda et al., 2010, their Suppl. Fig. 3) could also contribute to modulate left S1 excitability.

The strong sensitization observed in the right cortices could be triggered by crossed, descending corticotrigeminal outflow from INS and S1 ophthalmic fields to left medullary Sp5C neurons. SD initiated within S1 or INS ophthalmic fields elicits inhibition and facilitation of meningeal over cutaneous nociceptive inputs onto Sp5C neurons, respectively. Also, SD initiated in V1 interrupts earlier S1 and then INS activities, eliciting inhibition followed by enhancement of meningeal-evoked responses of Sp5C neurons (Noseda et al., 2010). Interestingly, the present study showed that SD affects first S1 then INS activities, suggesting that such lateralized corticotrigeminal outflow could contribute to specific tuning of headache pain during a migraine attack.

The bilateral effects of SD observed in the present study would thus result from complex interactions between top-down corticotrigeminal influences acting as modulators on Sp5C neurons, once the triggering of migraine pain was produced by bottom-up direct activation of meningeal nociceptors.

We used here percutaneous periorbital instead of meningeal stimulation for avoiding sensitization of meningeal nociceptors by the surgical procedures necessary to access to the dura. This stimulation procedure was also chosen because animal and human studies showed that the progressive increases of responses of thalamic neurons to periorbital and extracephalic skin stimulation reflect an index of central sensitization related to sustained headache pain (Burstein et al., 2010).

The preventive effects of the NMDA antagonist Memantine on rCBV increases elicited by SD also support the idea that these changes could represent a relevant marker of central sensitization of nociceptive origin as this phenomenon is dependent on glutamatergic transmission (Basbaum et al., 2009; Latremoliere and Woolf, 2009). This is suggested also by our findings showing that before SD. Memantine is unable to modify basal rCBV, but it fully antagonizes the increases in basal S1 and INS activities after SD. Memantine reduces also periorbital-evoked rCBV increases in S1 and INS elicited by SD. S1 ΣLFP increases in basal activities by SD were also completely antagonized by Memantine. These findings suggest that facilitation of basal and periorbital rCBV-evoked activities in both S1 and INS by SD are highly dependent on NMDA-related mechanisms. On the other hand, the effects on neuronal periorbital-evoked activities have been revealed to be more complex. Before SD induction, SEP periorbital-evoked activities were reduced by Memantine in S1, in agreement with the well-known NMDA-dependent neuronal activation following repetitive percutaneous electrical stimulation (Basbaum et al., 2009; Latremoliere and Woolf, 2009). However, after SD, Memantine administration was unable to depress the increases in periorbital-evoked SEP activities. This could be because of its uncompetitive NMDA antagonist profile with moderate affinity (Parsons et al., 1999) or to the emergence of additional, non-NMDA sensitization mechanisms that are probably brought into play.

Memantine was chosen for its inhibitory effects on SD onset in the neocortex (Peeters et al., 2007) brainstem of rats (Jansen et al., 2019) and isolated chick retina (Kertesz et al., 2010). Clinical studies showed that compared with other NMDA antagonists, Memantine is well tolerated in preventive trials and significantly reduces aura and migraine headache with few side effects (Charles et al., 2007; Bigal et al., 2008; Afridi et al., 2013; Noruzzadeh et al., 2016). Also, the recent use of Memantine for NMDA antagonism targeting SD inhibition in brain slices and in a clinical case suggest that Memantine could be considered for future clinical trials as an alternative to ketamine in brain injury patients because of its lack of ketamine side effects limiting its use (Reinhart et al., 2021).

Cortical pain matrix sensitization following SD appears here as a sequential maladaptive plasticity process that progressively turns trigeminovascular nociceptive networks into a novel, dysfunctional state. Although the single SD wave triggered from V1 exhibits a unilateral spread, our findings show that its effects in cortical plasticity are bilateral but not identical, involving NMDA processing mechanisms. It is possible that during migraine headache a complex interplay occurs between bottom-up peripheral activation and top-down cortical modulation mechanisms. As previously argued (Dreier and Reiffurth, 2015), such complexity and the clinical observations make a simple cause-effect relationship between SD and migraine headache further unlikely.

Our findings support the operational usefulness of combining fUS imaging with electrophysiological studies as a tool for assessing nociceptive maladaptive plasticity mechanisms at different levels of the cortical pain matrix. This model provides a widespread observation post for assessing craniofacial neurovascular coupling and uncoupling mechanisms involved in headache signaling. Further studies in awake rodents are necessary for avoiding artifacts introduced by the acute surgical procedures and general anesthesia used here, and experiments including neuronal, glial manipulation, females, and genetic models of migraine are also necessary.

References

Afridi SK, Giffin NJ, Kaube H, Goadsby PJ (2013) A randomized controlled trial of intranasal ketamine in migraine with prolonged aura. Neurology 80:642–647.

Anzabi M, Baoqiang L, Wang H, Kura S, Sakadzic S, Boas D, Stergaard L, Ayata C (2021) Optical coherence tomography of arteriolar diameter and capillary perfusion during spreading depolarizations. J Cereb Blood Flow Metab 41:2256–2263.

Aurora SK, Wilkinson F (2007) The brain is hyperexcitable in migraine. Cephalalgia 27:1442–1453.

Basbaum AI, Bautista DM, Scherrer G, Julius D (2009) Cellular and molecular mechanisms of pain. Cell 139:267–284.

Bigal M, Rapoport A, Sheftell F, Tepper D, Tepper S (2008) Memantine in the preventive treatment of refractory migraine. Headache 48:1337–1342.

Boido D, Rungta RL, Osmanski BF, Roche M, Tsurugizawa T, Le Bihan D, Ciobanu L, Charpak S (2019) Mesoscopic and microscopic imaging of sensory responses in the same animal. Nat Comm 10:1110.

Bolay H, Reuter U, Dunn AK, Huang Z, Boas DA, Moskowitz MA (2002) Intrinsic brain activity triggers trigeminal meningeal afferents in a migraine model. Nat Med 8:136–142.

Borsook D, Veggeberg R, Erpelding N, Borra R, Linnman C, Burstein R, Becerra L (2016) The insula: a "hub of activity" in migraine. Neuroscientist 22:632–652.

Brennan KC, Pietrobon D (2018) A systems neuroscience approach to migraine. Neuron 97:1004–1021.

Burstein R, Jakubowski M, Garcia-Nicas E, Kainz V, Bajwa Z, Hargreaves R, Becerra L, Borsook D (2010) Thalamic sensitization transforms localized pain into widespread allodynia. Ann Neurol 68:81–91.

Chang JC, Shook LL, Biag J, Nguyen EN, Toga AW, Charles AC, Brennan KC (2010) Biphasic direct current shift, haemoglobin desaturation and neurovascular uncoupling in cortical spreading depression. Brain 133:996–1012.

Charles A, Flippen C, Romero Reyes M, Brennan KC (2007) Memantine for prevention of migraine: a retrospective study of 60 cases. J Headache Pain 8:248–250.

Charles AC, Baca SM (2013) Cortical spreading depression and migraine. Nat Rev Neurol 9:637–644.

Coppola G, Pierelli F, Schoenen J (2007) Is the cerebral cortex hyperexcitable or hyperresponsive in migraine? Cephalalgia 27:1427–1439.

Craig AD (2014) Topographically organized projection to posterior insular cortex from the posterior portion of the ventral medial nucleus in the long-tailed macaque monkey. J Comp Neurol 522:36–63.

Deffieux T, Demene C, Pernot M, Tanter M (2018) Functional ultrasound neuroimaging: a review of the preclinical and clinical state of the art. Curr Opin Neurobiol 50:128–135.

Demené C, Deffieux T, Pernot M, Osmanski BF, Biran V, Gennisson JL, Sieu LA, Bergel A, Franqui S, Correas JM, Cohen I, Baud O, Tanter M (2015) Spatiotemporal clutter filtering of ultrafast ultrasound data highly increases doppler and fultrasound sensitivity. IEEE Trans Med Imaging 34:2271–2285.

Dreier JP, Reiffurth C (2015) The stroke-migraine depolarization continuum. Neuron 86:902–922.

Eckhorn R, Thomas U (1993) A new method for the insertion of multiple microprobes into neural and muscular tissue, including fiber electrodes, fine wires, needles and microsensors. J Neurosci Methods 49:175–179.

Hadjikhani N, Sanchez Del Rio M, Wu O, Schwartz D, Bakker D, Fischl B, Kwong KK, Cutrer FM, Rosen BR, Tootell RB, Sorensen AG, Moskowitz MA (2001) Mechanisms of migraine aura revealed by functional MRI in human visual cortex. Proc Natl Acad Sci U S A 98:4687–4692.

Jansen NA, Schenke M, Voskuyl RA, Thijs RD, Van den Maagdenberg AMJM, Tolner EA (2019) Apnea associated with brainstem seizures in Cacna 1a mice is caused by medullary spreading depolarization. J Neurosci 39:9633– 9644.

Jia Z, Yu S, Tang W, Zhao D (2020) Altered functional connectivity of the insula in a rat model of recurrent headache. Mol Pain 16:1744806920922115.

Kayser C, Kim M, Ugurbil K, Kim DS, König P (2004) A comparison of hemodynamic and neural responses in cat visual cortex using complex stimuli. Cereb Cortex 14:881–891.

Kertesz S, Kapus G, Gacsalyi I, Levay G (2010) Deramciclane improves object recognition in rats: potential role of NMDA receptors. Pharmacol Biochem Behav 94:570–574.

Latremoliere A, Woolf CJ (2009) Central sensitization: a generator of pain hypersensitivity by central neural plasticity. J Pain 10:895–926.
Lauritzen M, Mathiesen C, Schaefer C, Thomsen KJ (2012) Neuronal inhibition and excitation, and the dichotomic control of brain hemodynamic and oxygen responses. Neuroimage 62:1040–1050.
Logothetis NK, Wandell BA (2004) Interpreting the BOLD signal. Annu Rev Physiol 66:735–769.
Logothetis NK, Pauls J, Augath M, Trinath T, Oeltermann A (2001) Neurophysiological investigation of the basis of the fMRI signal. Nature 412:150–157.
Macé E, Montaldo G, Cohen I, Baulac M, Fink M, Tanter M (2011) Functional ultrasound imaging of the brain. Nat Methods 8:662–664.
Masamoto K, Kim T, Fukuda M, Wang P, Kim SG (2007) Relationship between neural, vascular, and BOLD signals in isoflurane-anesthetized rat somatosensory cortex. Cereb Cortex 17:942–950.
Mathiesen C, Caesar K, Lauritzen M (2000) Temporal coupling between neuronal activity and blood flow in rat cerebellar cortex as indicated by field potential analysis. J Physiol 523:235–246.
Niessing J, Ebisch B, Schmidt KE, Niessing M, Singer W, Galuske RA (2005) Hemodynamic signals correlate tightly with synchronized gamma oscillations. Science 309:948–951.
Noruzzadeh R, Modabbernia A, Aghamollaii V, Ghaffarpour M, Harirchian MH, Salahi S, Nikbakht N, Noruzi N, Tafakhori A (2016) Memantine for prophylactic treatment of migraine without aura: a randomized double-blind placebo-controlled study. Headache 56:95–103.
Noseda R, Burstein R (2013) Migraine pathophysiology: anatomy of the trigeminovascular pathway and associated neurological symptoms, CSD, sensitization and modulation of pain. Pain 154:S44–S53.
Noseda R, Monconduit L, Constandil L, Chalus M, Villanueva L (2008) Central nervous system networks involved in the processing of meningeal and cutaneous inputs from the ophthalmic branch of the trigeminal nerve in the rat. Cephalalgia 28:813–824.
Noseda R, Constandil L, Bourgeais L, Chalus M, Villanueva L (2010) Changes of meningeal excitability mediated by corticotrigeminal networks: a link for the endogenous modulation of migraine pain. J Neurosci 30:14420–14429.
Olesen J, Friberg L, Olsen TS, Iversen HK, Lassen NA, Andersen AR, Karle A (1990) Timing and topography of cerebral blood flow, aura, and headache during migraine attacks. Ann Neurol 28:791–798.
Parker PD, Suryavanshi P, Melone M, Sawant Pokam PA, Reinhart KM, Kaufmann D, Theriot JJ, Pugliese A, Conti F, Shuttleworth CW, Pietrobon D, Brennan KC (2021) Non-canonical glutamate signaling in a genetic model of migraine with aura. Neuron 109:611–618.
Parsons CG, Danysz W, Quack G (1999) Memantine is a clinically well tolerated N-methyl-D-aspartate (NMDA) receptor antagonist–a review of preclinical data. Neuropharmacology 38:735–767.
Paxinos G, Watson C (1998) The rat brain in stereotaxic coordinates. San Diego: Academic.
Peeters M, Gunthorpe MJ, Strijbos PJ, Goldsmith P, Upton N, James MF (2007) Effects of pan- and subtype-selective N-methyl-D-aspartate receptor antagonists on cortical spreading depression in the rat: therapeutic potential for migraine. J Pharmacol Exp Ther 321:564–572.
Piilgaard H, Lauritzen M (2009) Persistent increase in oxygen consumption and impaired neurovascular coupling after spreading depression in rat neocortex. J Cereb Blood Flow Metab 29:1517–1527.
Provansal M, Labermede G, Joffrois C, Rizkallah A, Goulet R, Valet M, Deschamps W, Ferrari U, Chaffio A, Dalkara D, Sahel J, Tanter M, Picaud S, Gauvain G, Arcizet F (2021) Functional ultrasound imaging of the spreading activity following optogenetic stimulation of the rat visual cortex. Sci Rep 11:12603.
Rabut C, Correia M, Finel V, Pezet S, Pernot M, Deffieux T, Tanter M (2019) 4D functional ultrasound imaging of whole-brain activity in rodents. Nat Methods 16:994–997.
Reinhart KM, Humphrey A, Brennan KC, Carlson AP, Shuttleworth CW (2021) Memantine improves recovery after spreading depolarization in brain slices and cans be considered for future clinical trials. Neurocrit Care 35(Suppl 2):135–145.
Sawant-Pokam PM, Suryavanshi P, Mendez JM, Dudek FE, Brennan KC (2017) Mechanisms of neuronal silencing after cortical spreading depression. Cereb Cortex 27:1311–1325.
Sieu LA, Bergel A, Tiran E, Deffieux T, Pernot M, Gennisson JL, Tanter M, Cohen I (2015) EEG and functional ultrasound imaging in mobile rats. Nat Methods 12:831–834.
Urban A, Mace E, Brunner C, Heidmann M, Rossier J, Montaldo G (2014) Chronic assessment of cerebral hemodynamics during rat forepaw electrical stimulation using functional ultrasound imaging. Neuroimage 101:138–149.
Vierck CJ, Whitsel BL, Favorov OV, Brown AW, Tommerdahl M (2013) Role of primary somatosensory cortex in the coding of pain. Pain 154:334–344.
Woods RP, Iacoboni M, Mazziotta JC (1994) Brief report: bilateral spreading cerebral hypoperfusion during spontaneous migraine headache. N Engl J Med 331:1689–1692.
Youssef AM, Ludwick A, Wilcox SL, Lebel A, Peng K, Colon E, Danehy A, Burstein R, Becerra L, Borsook D (2017) In child and adult migraineurs the somatosensory cortex stands out ... again: an arterial spin labeling investigation. Hum Brain Mapp 38:4078–4087.
Zhang X, Levy D, Noseda R, Kainz V, Jakubowski M, Burstein R (2010) Activation of meningeal nociceptors by cortical spreading depression: implications for migraine with aura. J Neurosci 30:8807–8814.
Zimmermann M (1983) Ethical guidelines for investigations of experimental pain in conscious animals. Pain 16:109–110.